

# Climate change induced uncertainties in phytoplankton spring bloom dynamics

Lőrinc Mészáros<sup>1,2,\*</sup>, Frank van der Meulen<sup>2</sup>, Geurt Jongbloed<sup>2</sup> and Ghada El Serafy<sup>1,2</sup>

<sup>1</sup>Marine and Coastal Systems, Deltares, Delft, The Netherlands

<sup>2</sup>Applied Mathematics, Delft University of Technology, Delft, The Netherlands

Correspondence\*:

Lőrinc Mészáros

Lorinc.Meszaros@deltares.nl

## 2 ABSTRACT

This paper aims to study the evolution of phytoplankton bloom dynamics in the Dutch coastal waters, using a variety of historical data and projected future solar radiation and air temperature trajectories from regional climate models as driving forces covering the 21<sup>st</sup> century. The main objective is to quantify climate induced uncertainties in future coastal phytoplankton phenology stemming from important climate variables. The three main methodological steps to achieve this goal include (1) developing a data fusion model to interlace coastal in-situ measurements and satellite chlorophyll-a observations into a single multi-decadal signal; (2) applying a Bayesian structural time series forecasting model to produce long-term prediction of chlorophyll-a concentrations over the 21<sup>st</sup> century; and (3) developing a feature extraction method to derive the cardinal dates (beginning, peak, end) of the spring bloom to track the historical and the projected evolution of its dynamics. Research findings indicate that at the study site location the spring bloom characteristics are impacted by the changing climatic conditions. Towards the end of the 21<sup>st</sup> century climatic factors may shift spring blooms slightly earlier, resulting in longer spring bloom duration. Moreover higher chlorophyll-a concentration peaks can be expected. Based on the ensemble simulation the largest uncertainty lies in the timing of the spring bloom beginning and -end timing, while the peak timing has less variation.

Keywords: regional climate model, climate change, uncertainty quantification, phytoplankton phenology, Bayesian model, data fusion, non-parametric regression

## 1 INTRODUCTION

Phytoplankton is the base of aquatic food webs and it plays a crucial role in the marine ecosystem by regulating biogeochemical cycles and production. Phytoplankton blooms are natural phenomena occurring when phytoplankton growth exceeds the losses (mortality and feeding) and rapid accumulation takes place, when optimal abiotic and biotic conditions are present for the growth. One can identify phytoplankton blooms through the evolution of chlorophyll-a concentration. This concentration is an indicator for algal biomass, though concerns were raised by [1] about using chlorophyll as phytoplankton biomass proxy in the North Sea. In the Dutch coastal zone, phytoplankton mass seasonality is described by a prominent spring bloom and a less pronounced late summer bloom. The onset of spring blooms is initiated by correlated changes in water temperature and the light availability [38]. Temperate marine environments, such as the Dutch coastal waters, are particularly sensitive to these changes due to the fact that higher trophic levels are greatly dependent on synchronized planktonic production [11]. Seasonal variability of phytoplankton biomass in relation to environmental conditions such as light and temperature is therefore an important aspect in the North West Shelf Seas [22]. The interactive effects of temperature and solar irradiance on phytoplankton have been extensively studied without clear consensus. This may be partly due to the fact that phytoplankton response to temperature change greatly varies between individual and aggregate level. Considering the individual level phytoplankton responses to temperature are exponentially or linearly increasing until the optimum, and declining above that [10]. On the other hand, looking at the aggregate level, species can replace one another along a temperature gradient via competition resulting in

monotonically increasing growth rates. In temperate marine systems, the impact of physical environment and the response of the biological system can be best studied in spring [30]. During spring, the physical limiting factors like temperature, light availability, and mixing are more prominent than the non-physical ones, such as nutrient availability and trophic interactions (e.g. grazing). Consequently, we focus on the spring phytoplankton bloom to study the impact of changing climatic conditions in the Dutch coastal zone.

Changing climatic conditions directly affect the photosynthetic metabolism of phytoplankton, but also indirectly impact them by modifying their physical environment [7]. Climate change impacts on phytoplankton are manifested as shifts in seasonal dynamics, species composition, and population size structure [38]. Since in the current study we only use chlorophyll-a concentration as response variable, we can only draw conclusions on the seasonal dynamics of the aggregate level, not on species composition or population structure. As an indicator of climate change impacts on seasonal phytoplankton dynamics, we selected the long term evolution of spring blooms. There is, however, no single definition of phytoplankton blooms in the literature or in policies, for instance based on the rate of change or the threshold of concentration, as this is highly dependent on the type of ecosystems (e.g. inland or marine, local species, climate, bathymetry). One might use the number of consecutive days that exceed a given threshold (elevated assessment level) defined by the literature. In the case of Dutch coastal waters this is around 12-15 mg/m<sup>3</sup> and 22-24 mg/m<sup>3</sup> for the Wadden Sea [26]. Alternatively, a low-pass method could be used for determining the start of the bloom [35], which is a temporal averaging algorithm acting as a low-pass filter, reducing the short-term fluctuations. [27] suggested using the date of the maximum and minimum values of daily change rates in the interpolated chlorophyll-a concentrations for the timing of the annual onset and breakdown of the phytoplankton bloom. The timing of the bloom can also be represented by another quantity, the center of gravity (COG) of the carbon content within the typical spring bloom period [16]. Another possibility to characterise the spring bloom is to derive the cardinal dates of the mass development [30]. The cardinal dates are the beginning of the spring phytoplankton mass development, the maximum of the spring bloom (bloom peak), and the end of the spring mass development. Mathematical methods of describing cardinal dates were proposed by [30], such as finding the points of inflection in the smoothed, log transformed, and differenced (1-week lag) data, deriving them from four linear segments (constant - increasing - decreasing - constant) fitted to the logarithmic values, or extracting the cardinal dates from the quantiles of a fitted parametric function (Weibull function). Similarly, [21] transformed phytoplankton biomass according to standard normal variation and took the first and third quartiles as cardinal dates, the beginning and the end of the spring bloom, respectively. In this study we also describe the spring bloom dynamics by their cardinal dates but we propose an alternative method to derive these dates using log-concave regression.

A range of studies investigating climate change induced shifts in phytoplankton bloom dynamics in the North Sea already exist. Most of these studies derive their findings from historical chlorophyll-a data, measured either by in-situ sensors or remote sensing [8, 16, 27, 11], or from laboratory experiments [21, 36]. Climate impact studies which focus on future developments of phytoplankton bloom dynamics generally use few climate change scenarios from global or regional climate models and traditionally use physically-based models [12, 17, 18, 28, 32]. We acknowledge that previous papers already introduced ways to characterize phytoplankton blooms [35, 27, 16, 30, 21]. Nevertheless, uncertainty quantification in the shift of phytoplankton dynamics in these studies is not a central topic. Considering the above, the novelty of our work lies in the following features. In our research we make use of both in-situ and satellite observations jointly by applying a data fusion algorithm to get a more complete, more accurate and longer data record. While a range of possibilities already exist to describe phytoplankton blooms, in our research we propose a new way of extracting the cardinal dates of the phytoplankton spring blooms (concave regression). Moreover, we complement existing climate change scenarios with synthetically generated ones, thus supplying numerous (> 100) trajectories for air temperature and solar radiation development. In addition to this, our proposed method replaces the computationally expensive numerical models for chlorophyll-a simulation with a data driven approach, using a Bayesian structural time series forecasting model. Replacing physically-based prediction models with statistical ones allows us to compute a large number of simulations and achieve better characterization of predictive uncertainties. These novelties bring scientific advances that enhance our understanding of ecological responses to variable climate change, and most importantly offer ways to quantify uncertainties associated to data and the statistical methods.

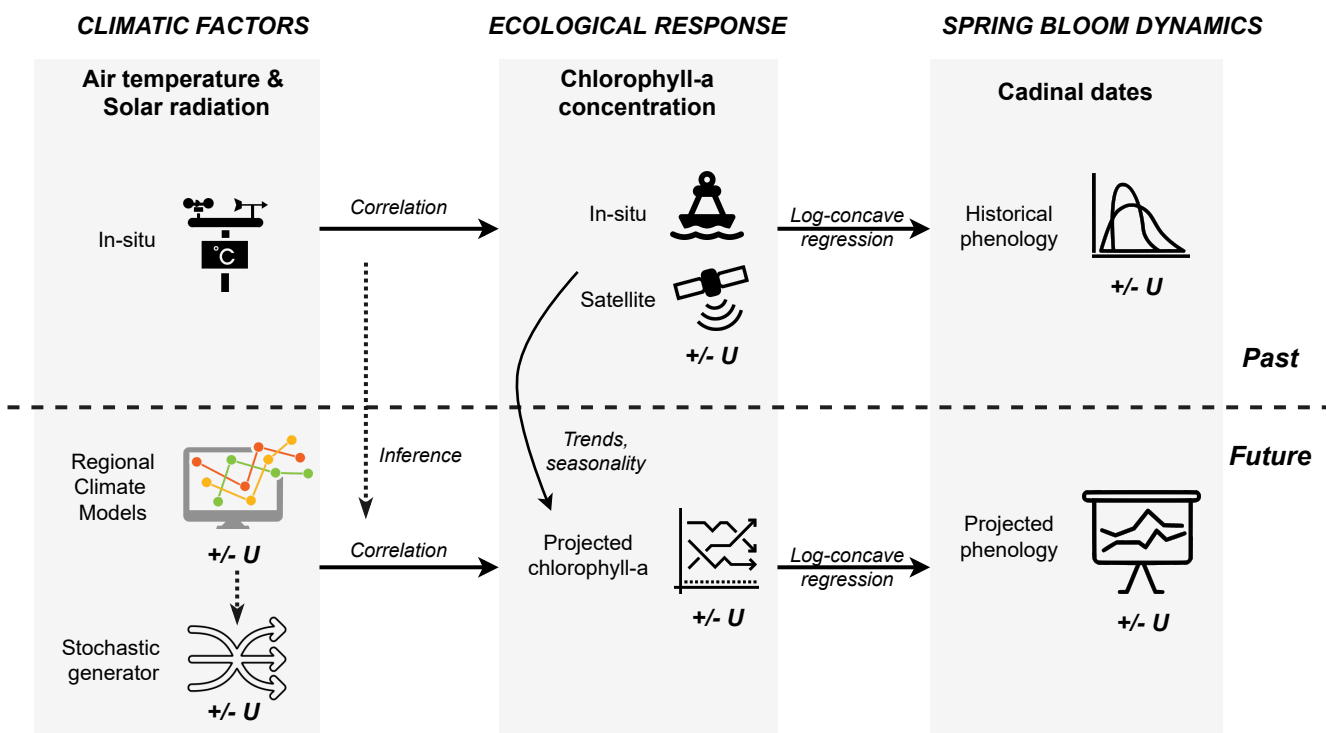


**Figure 1.** Methodological framework

## 2 MATERIALS AND METHODS

In short, this research aims to study changes in phytoplankton phenology based on historical data and future climate projections. In order to achieve this, the methodological framework includes three main elements with causal and temporal relations: (1) climatic factors, (2) ecological response, and (3) spring bloom dynamics (see Figure 1). Given the historical records of chlorophyll-a concentrations obtained from various data sources, one can extract the cardinal dates of the spring bloom for the past decades using the proposed feature extraction technique. Furthermore, changes in the spring blooms may be projected for the future by utilizing the correlation between climatic factors, represented by air temperature and solar radiation, and the ecological response, indicated by the chlorophyll-a concentration. This correlation can be inferred from past records since air temperature and solar radiation were measured by field sensors for the past decades. Though future chlorophyll-a concentrations are not available to us, we attempt to make projections using the trends and seasonality from historical observations and taking into account the correlations with projected air temperature and solar radiation, produced by regional climate models. While this methodological framework allows us to investigate past and projected spring bloom dynamics, we note that there are several sources of uncertainties, both data and model related ones, which are propagated through the steps. These uncertainty sources (+/- U) are marked in Figure 1. In order to address this issue, we aim to use transparent statistical approaches that allow us to quantify intrinsic uncertainties. The uncertainty quantification framework is at the very core of this research, which should always go hand-in-hand with climate change impact studies.

### 2.1 Data sources

This research is based on a multitude of data sources from sensors and numerical models of various types. The environmental and climate variables in this study are chlorophyll-a concentration, air temperature, and solar radiation. In order to investigate past trends and obtain the correlation between these variables, we make use of historical measurements, whereas to anticipate future climate change impacts, climate model outputs are used.

#### 2.1.1 Chlorophyll-a concentration measurements

Available historical chlorophyll-a data includes field observations at Marsdiep Noord station, from the Dutch Directorate-General for Public Works and Water Management (Rijkswaterstaat), covering more than forty years from 1976 to 2018, but measured rather sparsely. To complement these field measurements,

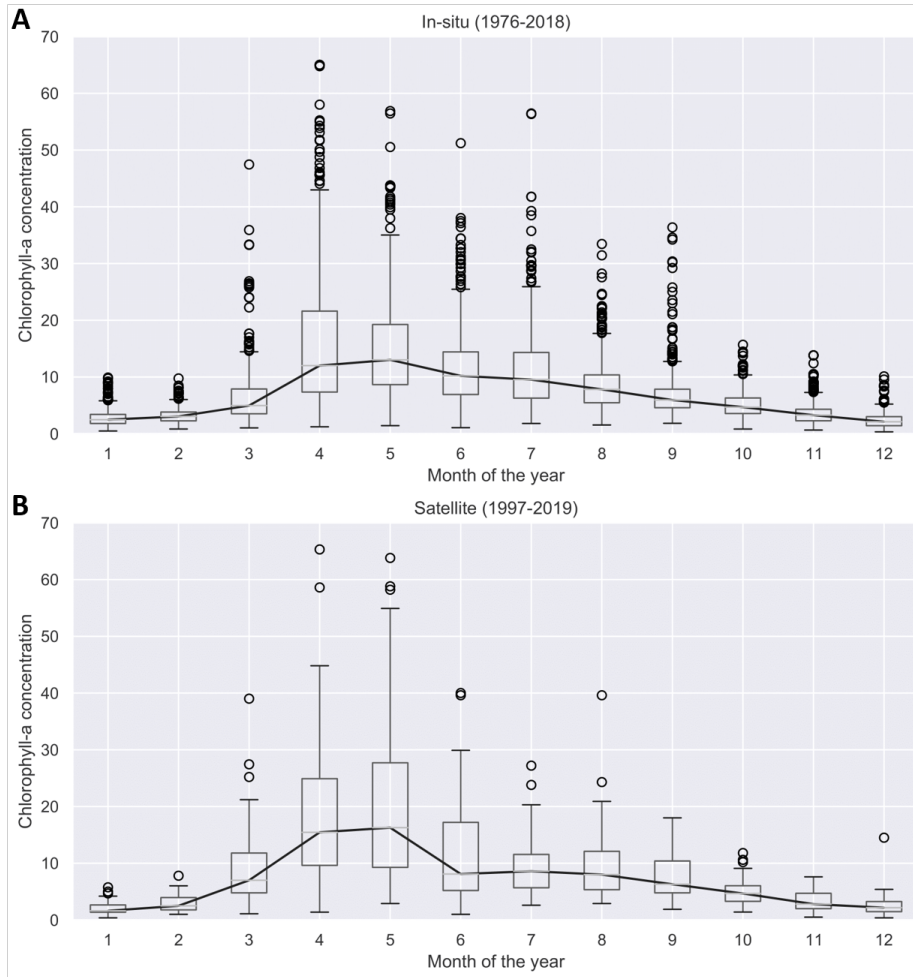


**Figure 2.** Historical chlorophyll-a concentrations measured in the Dutch Wadden Sea using in-situ data between 1976-2018 (**A**) and satellite images between 1997-2019 (**B**). Climatological median (solid black line) per calendar is also shown.

120 processed and validated satellite observed chlorophyll-a concentration (extracted at the same location) was  
 121 used from the Copernicus Marine Environment Monitoring Service (CMEMS) from 1997 to 2019. The  
 122 specific product in use is the North Atlantic Chlorophyll-a (Copernicus-Globcolour), daily interpolated  
 123 and reprocessed product with one km spatial resolution. The chlorophyll-a concentration seasonality from  
 124 in-situ observation is shown in Figure 2A, and from satellite observations in Figure 2B.

125 Naturally these data sources have different temporal resolutions and associated uncertainties. In-situ  
 126 observations are often considered as ground truth and are the most reliable, however, in the case of  
 127 chlorophyll-a concentration the temporal frequency of the observations is relatively low, around 10-20  
 128 observations per year. This monthly sampling frequency has a limitation to assess annual phytoplankton  
 129 bloom cycles [37]. Thus, the more frequently sampled satellite images are also used to complement the  
 130 in-situ measurements for a better assessments of bloom characteristics. This complementary data source  
 131 is used noting that satellite derived chlorophyll-a has a higher level of associated uncertainty. Since the  
 132 two types of chlorophyll-a measurements describe the same underlying process, we propose a data fusion  
 133 model to combine them. This data fusion model interlaces the in-situ and satellite observations into a single  
 134 chlorophyll-a concentration signal, which is more complete then the individual observations and covers a  
 135 longer time period. The data fusion model is described in Section 2.2.  
 136

### 2.1.2 Solar radiation and air temperature measurements

137 The historical daily solar radiation and air temperature records are obtained at the nearest weather  
 138 station (De Kooy) from the Royal Netherlands Meteorological Institute (KNMI) for the matching period

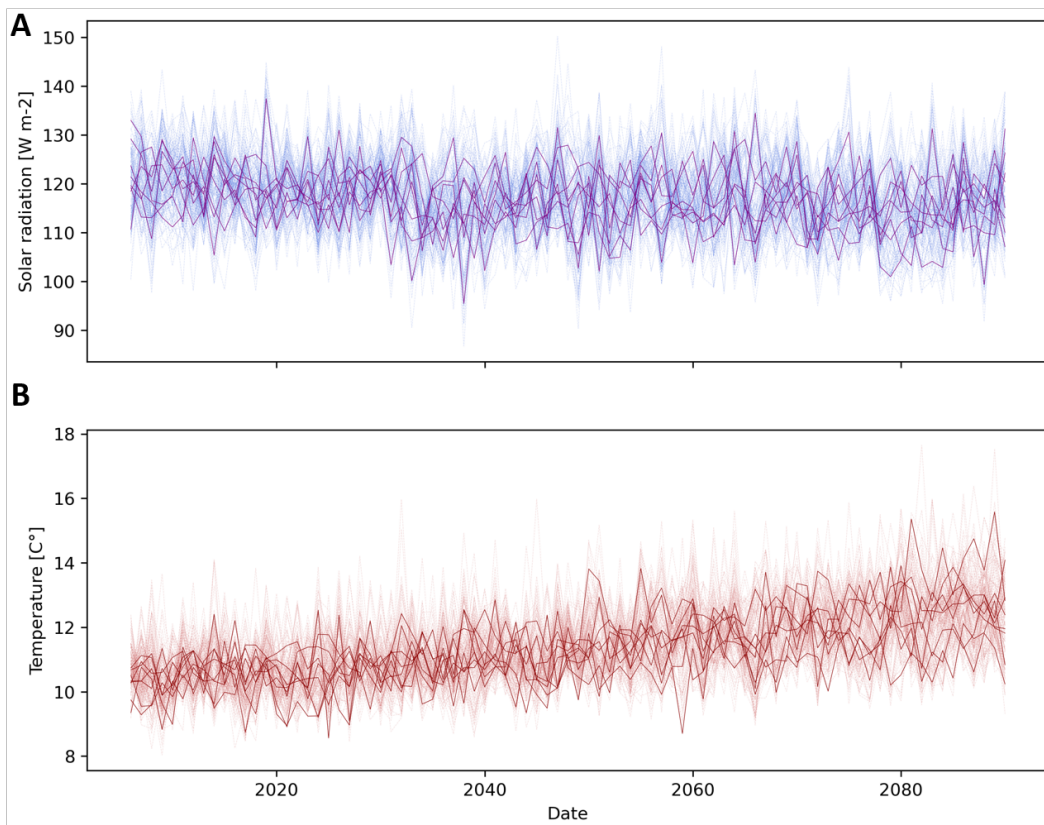


**Figure 3.** Eight Euro-CORDEX (darker solid line) and 120 generated synthetic (shaded dashed line) climate change projections for solar radiation (**A**) and air temperature (**B**). Plot of the yearly averages based on the daily data.

139 (1976-2019). Apart from historical data, future projected values of air temperature and solar radiation  
 140 are acquired from the high resolution 0.11 degree ( $\sim 12.5$  km) EURO-CORDEX Coordinated Regional  
 141 Downscaling Experiment [19], which uses the Swedish Meteorological and Hydrological Institute Rossby  
 142 Centre regional atmospheric model (SMHI-RCA4). In order to produce various regionally downscaled  
 143 scenarios, EURO-CORDEX applies a range of General Circulation Models (GCMs) to drive the above  
 144 mentioned Regional Climate Model (RCM). In addition to the driving models, further scenarios are  
 145 obtained by considering different socio-economic changes described in the Representative Concentration  
 146 Pathways (RCPs). RCPs are labeled according to their specific radiative forcing pathway in 2100 relative  
 147 to pre-industrial values. In this study we include RCP8.5 (high), and RCP4.5 (medium-low) [34] and four  
 148 driving GCMs. Together the four different driving GCMs and two RCPs provide us with an ensemble  
 149 of eight future solar radiation and temperature trajectories. Since the RCM simulations are subject to  
 150 climate model structural error and boundary errors from the driving GCMs [25], they should be bias  
 151 corrected before applying them in impact studies [23]. For this reason, quantile mapping bias correction  
 152 [2] was applied using the RCM simulations for the reference period (1976-2005) and daily historical  
 153 field measurements from KNMI for the same period, as described in [24]. The quantile-quantile mapping  
 154 transfer functions were established for the reference period and separately for each RCM simulation.  
 155 The transfer functions were then applied for the bias correction of each future projections (2006-2100)  
 156 separately.

157 This ensemble of climate trajectories is used to simulate a range of possible phytoplankton seasonality  
 158 shifts and the associated uncertainty described by the predictive distribution of the phytoplankton bloom  
 159 cardinal dates. It should be noted that applying only eight climate projections reduces the ability to  
 160 adequately resolve the unknown predictive distribution that one tries to estimate, hence, higher number of  
 161 climate trajectories providing sufficient resolution in terms of probabilities is required [20]. Consequently,  
 162 to better characterize uncertainties, an enriched set of climate change projections is employed. This set of

air temperature and solar radiation projections was produced using a Bayesian stochastic generator [24], which builds on the above mentioned Regional Climate Model scenarios provided by the EURO-CORDEX experiment and generates further synthetic scenarios using a hierarchical Bayesian model. The generated ensemble of air temperature and solar radiation projections include 120 members and their statistical properties are similar to the input projections. Both the Euro-CORDEX and synthetic projections are shown for air temperature in Figure 3A and for solar radiation in Figure 3B. At this specific location we can observe a consistently increasing temperature trend over the 21<sup>st</sup> century and a slightly decreasing solar radiation trend. While increasing air temperatures are in line with expectations, decreasing solar radiation trends may need further explanation. The main cause of this negative trend is the fact that total cloud cover at this site is projected by Euro-CORDEX to increase, hence, limiting surface downwelling shortwave radiation. This is a region specific feature, and the difficulty of projecting cloud cover and solar radiation changes in coastal areas with sea-land-atmosphere boundaries, such as the study site, has been previously highlighted by [4], along with discrepancy between RCMs and their driving GCMs in their solar radiation projections over Europe.

## 2.2 Data fusion of chlorophyll-a measurements

### 2.2.1 Statistical model

In order to describe the chlorophyll-a concentration, we assume that there is a continuously evolving latent signal ( $X_t$ ,  $t \in [0, T]$ ) that satisfies the stochastic differential equation (sde)

$$dX_t = -\alpha(X_t - \mu(t)) dt + \sigma dW_t. \quad (1)$$

The underlying idea is to model a stochastic process that is mean reverting (with strength  $\alpha$ ) towards the deterministic signal  $t \mapsto \mu(t)$ . We will take  $\mu$  to be periodic with period 1. We start off from a continuous time description as in-situ measurements are not collected at regular times. Observations can be of three types

- 1.  $Y_i \sim N(X_{t_i}, \psi_1)$ ;
- 2.  $Y_i \sim N(X_{t_i}, \psi_2)$ ;
- 3.  $Y_i \sim N_2 \left( \begin{bmatrix} 1 \\ 1 \end{bmatrix} X_{t_i}, \begin{bmatrix} \psi_1 & 0 \\ 0 & \psi_2 \end{bmatrix} \right)$ .

This reflects having two types of measurements (in-situ and satellite) with different accuracies. Sometimes one measurement is obtained, sometimes the other one, and sometimes both are available.

Assuming successive observations are obtained closely in time, i.e.  $\Delta_i := t_i - t_{i-1}$  being small for all  $i$ , we have

$$X_{t_i} \approx X_{t_{i-1}} - \alpha(X_{t_{i-1}} - \mu(t_{i-1}))\Delta_i + \sigma\sqrt{\Delta_i}\epsilon_i,$$

where  $\{\epsilon_i\}_i$  is a sequence of independent standard Normal random variables. Ignoring discretisation error, the resulting equation can be rewritten and combined with the observation scheme:

$$\begin{aligned} X_i &= (1 - \alpha\Delta_i)X_{i-1} + \alpha\mu(t_{i-1})\Delta_i + \sigma\sqrt{\Delta_i}\epsilon_i \\ Y_i &= N(L_i X_i, \Upsilon_i), \end{aligned}$$

where  $X_i \equiv X_{t_i}$ . For numerical stability, it is better to discretise (1) using an implicit scheme on the deterministic part. This leads to the dynamical system

$$\begin{aligned} X_i &= \frac{X_{i-1} + \alpha\mu(t_i)\Delta_i}{1 + \alpha\Delta_i} + \sigma\sqrt{\Delta_i}\epsilon_i \\ Y_i &= N(H_i X_i, R_i), \end{aligned}$$

We write the model in state-space form, sticking to the notation in Särkka [31]

$$\begin{aligned} X_i &= A_{i-1}X_{i-1} + a_{i-1} + N(0, Q_{i-1}) \\ Y_i &= H_i X_i + N(0, R_i) \end{aligned} \quad (2)$$

193 Here

$$A_{i-1} = (1 + \alpha\Delta_i)^{-1} \quad a_{i-1} = \frac{\alpha\Delta_i}{1 + \alpha\Delta_i}\mu(t_i) \quad Q_{i-1} = \sigma^2\Delta_i,$$

194

$$R_i = \begin{cases} \psi_1 & \text{if only in-situ measurement} \\ \psi_2 & \text{if only satellite measurement} \\ \begin{bmatrix} \psi_1 & 0 \\ 0 & \psi_2 \end{bmatrix} & \text{both in-situ and satellite measurements} \end{cases}$$

195 and

$$H_i = \begin{cases} \begin{bmatrix} 1 \\ 1 \end{bmatrix}' & \text{if only 1 measurement is available at time } t_i \\ \begin{bmatrix} 1 & 1 \end{bmatrix}' & \text{if both measurements are available at time } t_i \end{cases}.$$

196 We take  $Y_i$  to be the log of the measured concentration (component-wise) to ensure the model only predicts  
 197 non-negative concentrations. While we acknowledge that there are other mapping functions to achieve  
 198 non-negativity, taking the log of chlorophyll-a concentration is often used in practice. We will parametrise  
 199  $\psi_1, \psi_2$  by taking

$$\psi_1 = \eta\bar{\psi}\psi \quad \psi_2 = \psi,$$

200 where  $\eta \in (0, 1)$  is fixed and  $\bar{\psi}$  will get assigned a prior distribution supported on  $(0, 1)$ . This reflects  
 201 apriori knowledge that the in-situ measurements are believed to be more accurate. This is even more so  
 202 important, as there are way more satellite measurements available than in-situ measurements and otherwise  
 203 the reconstruction would be mostly determined by the former measurements.

204 For  $\mu$  we propose a series expansion of the form

$$\mu(x) = \sum_{k=1}^K \xi_k \varphi_k(x),$$

205 where  $K$  is fixed, and  $\xi := (\xi_1, \dots, \xi_K) \sim N_K(0, \sigma_\xi^2 I)$ . The functions  $\varphi_k$  are taken as follows:  $\varphi_1 = \mathbf{1}_{[0,1]}$   
 206 and for  $j \in \{1, \dots, J\}$

$$\varphi_{jk}(x) = j^{-1} \varphi_0(2^{j-1}x - k), \quad \text{with } k \in \{0, \dots, 2^{j-1} - 1\}.$$

207 We take

$$\varphi_0(x) = \frac{9}{2}x^2\mathbf{1}_{[0,1/3]}(x) + \left(\frac{3}{4} - 9(x - 1/2)^2\right)\mathbf{1}_{[1/3,2/3]}(x) + \frac{9}{2}(1-x)^2\mathbf{1}_{[2/3,1]}(x),$$

208 which is the quadratic B-spline function scaled to have support  $[0, 1]$ . Note that  $\varphi_0$  is continuously  
 209 differentiable. The hierarchical structure of the basis is exactly like the Schauder basis, but uses a smoother  
 210 basic element than the traditional ‘‘hat’’-function.

## 2.2.2 Inference

212 Note that (2) specifies a linear Gaussian state-space model. The equation for  $Y$  is the observation equation,  
 213 that for  $X$  the state-equation. Let  $\theta = (\alpha, \xi, \sigma^2, \psi, \bar{\psi})$ . Inference can be carried out by initialising  $\theta$  and  
 214 iterating the following steps:

- 215 1. conditional on  $\theta, Y_1, \dots, Y_n$ , run the Forward Filtering Backwards Sampling (FFBS)-algorithm (see  
 216 Appendix) to reconstruct  $X_1, \dots, X_n$ ;
- 217 2. draw from the posterior of  $\theta$ , conditional on  $X_1, \dots, X_n$  and  $Y_1, \dots, Y_n$  (note that the likelihood is  
 218 simple, once we know the latent path  $X_1, \dots, X_n$ ).

219 For updating parameters we use Gibbs sampling. Note that the updates for  $\bar{\psi}$  and  $\psi$  only depend on  
 220  $Y_1, \dots, Y_n$  and updates for all other parameters only depend on  $X_1, \dots, X_n$ .

- 221 • The updates steps for  $\sigma^2$  and  $\psi$  are trivial when using independent InverseGamma distributions as prior  
 222 due to partial conjugacy.

- 223 • For  $\bar{\psi}$  we assume the  $Unif(0, 1)$ -prior. A Metropolis-Hastings step is implemented where we use  
 224 random-walk type proposals [29] of the form

$$\log \frac{\bar{\psi}^o}{1 - \bar{\psi}^o} := \log \frac{\bar{\psi}}{1 - \bar{\psi}} + N(0, \tau_{\bar{\psi}}^2),$$

225 which implies that the proposal ratio equals

$$\frac{q(\bar{\psi} | \bar{\psi}^o)}{q(\bar{\psi}^o | \bar{\psi})} = \frac{\bar{\psi}^o(1 - \bar{\psi}^o)}{\bar{\psi}(1 - \bar{\psi})}.$$

226 Note that  $\bar{\psi}^o = \bar{\psi}/(\bar{\psi} + (1 - \bar{\psi})\tau_{\bar{\psi}}Z)$ , where  $Z \sim N(0, 1)$ .

- 227 • For updating  $\alpha$  we use a Metropolis-Hastings step of the form  $\log \alpha^o := \log \alpha + N(0, \tau_{\alpha}^2)$ .  
 • The “full” conditional density for  $\xi$  is proportional to

$$\begin{aligned} & \exp \left( -\frac{1}{2\sigma_{\xi}^2} \|\xi\|^2 - \frac{1}{2\sigma^2} \sum_{i=2}^n \Delta_i^{-1} \left( X_i - A_{i-1}X_{i-1} - \frac{\alpha\Delta_i}{1+\alpha\Delta_i} \sum_{k=1}^K \xi_k \varphi_k(t_i) \right)^2 \right) \\ &= \exp \left( -\frac{1}{2\sigma_{\xi}^2} \|\xi\|^2 - \frac{1}{2\sigma^2} \sum_{i=2}^n \left( U_i - \bar{\alpha}_i \sum_{k=1}^K \xi_k \varphi_k(t_i) \right)^2 \right), \end{aligned}$$

228 where

$$U_i = \Delta_i^{-1/2} (X_i - A_{i-1}X_{i-1}) \quad \bar{\alpha}_i = \frac{\alpha\sqrt{\Delta_i}}{1+\alpha\Delta_i}.$$

229 This is proportional to

$$\exp \left( \left( -\frac{1}{2} \xi' (\sigma^{-2} V + \sigma_{\xi}^{-2} I_K) \xi + \sigma^{-2} \mathbf{v}' \xi \right) \right)$$

230 with

$$\mathbf{v}_k = \sum_{i=2}^n U_i \bar{\alpha}_i \varphi_k(t_i) \quad V_{k\ell} = \sum_{i=2}^n \bar{\alpha}_i^2 \varphi_k(t_i) \varphi_{\ell}(t_i).$$

231 Hence, the update step for  $\xi$  boils down to sampling from a multivariate normal distribution with  
 232 precision  $\sigma^{-2}V + \sigma_{\xi}^{-2}I_K$  and potential vector  $\sigma^{-2}\mathbf{v}$  (the potential vector is the product of the precision  
 233 matrix with the mean vector).

234 *Details on the prior specification:* for both  $\sigma^2$  and  $\psi$  we took (independently) InverseGamma priors with  
 235 both parameters equal to 0.1. For  $\alpha$  we took the Exponential distribution with mean 10. We took  $\sigma_{\xi}^2 = 10$   
 236 and tuned the step-sizes  $\tau_{\psi}$  and  $\tau_{\alpha}$  such that the corresponding random-walk Metropolis-Hastings steps  
 237 were accepted with probability in between 25% and 50%. In the series expansion we took a fixed value for  
 238 K=5. We took  $\eta = 658/8005$ , which is the ratio of the in-situ and satellite measurements.

### 239 2.2.3 Fused chlorophyll-a concentration signal

240 The fused chlorophyll-a concentration signal, together with satellite observations, is depicted in Figure  
 241 4A and with in-situ observations in Figure 4B. One can observe that the fused signal almost perfectly  
 242 follows the in-situ (“water”) observations over the period in which only that type of measurements are  
 243 available. From the moment that both in-situ and satellite date are available (1998), the fused signal lies  
 244 between the two types but being closer to the in-situ observations according to the model formulation, since  
 245 we have higher confidence in the field data. This is also reflected in the quantile-quantile plot of the fused  
 246 signal compared to the in-situ data in Figure 4C, which lies almost perfectly on the diagonal, whereas the  
 247 quantile-quantile plot of the fused signal against the satellite observations deviates more from the diagonal.

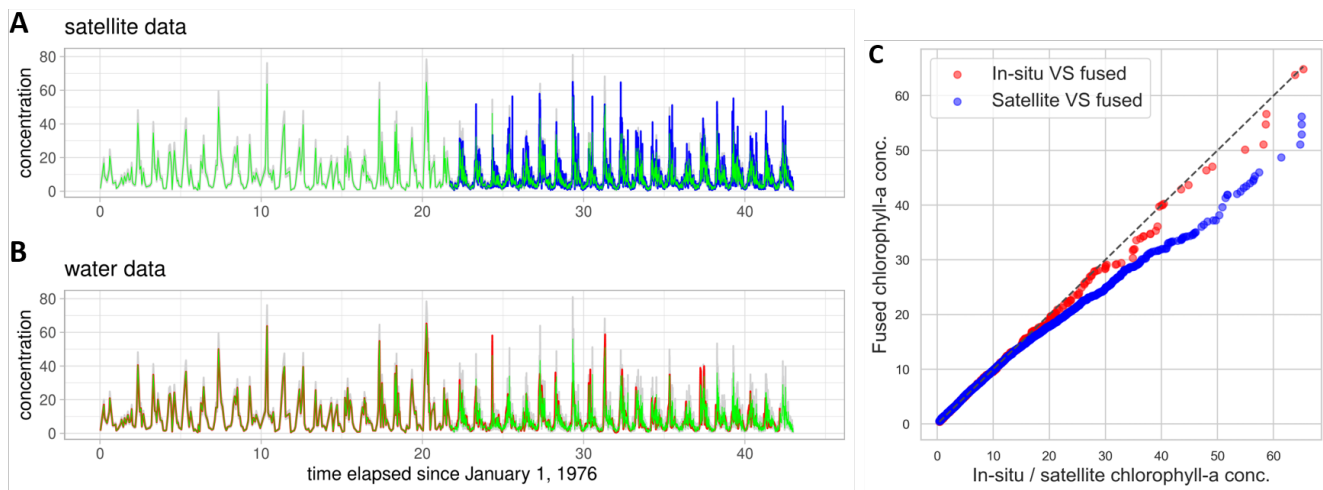


**Figure 4.** Data fusion results. The mean fused chlorophyll-a concentration signal (green) with uncertainty (grey) compared with satellite observations (blue) in (A), and in-situ "water" observations (red) in (B). Quantile-quantile plot of the fused signal compared to both in-situ and satellite observations in (C).

### 248 2.3 Long term prediction using Bayesian structural time series models

249 After the fused historical chlorophyll-a concentration signal has been derived, it is used to train the time  
 250 series forecasting model for long-term prediction. It was previously argued that variability in the spring  
 251 bloom dynamics occur due to changing environmental conditions. Consequently, apart from historical  
 252 trends and seasonality in the observed chlorophyll-a concentration time series, projected solar radiation  
 253 and air temperature are also used to drive the evolution of future chlorophyll-a concentration trajectories.  
 254 These simulated trajectories are then utilized to extract the long term evolution of bloom characteristics  
 255 applying the feature extraction methodology described in section 2.4.

#### 256 2.3.1 Bayesian structural time series model

257 Bayesian structural time series models possess three key features for modelling time series data that  
 258 are favorable for long-term chlorophyll-a concentration forecasting. The main feature is uncertainty  
 259 quantification, as they allow us to quantify the posterior uncertainty of the individual components, control  
 260 the variance of the components, and impose prior beliefs on the model. This is crucial as uncertainties  
 261 increase over time in the future, especially in long-term forecasting. The second key feature is transparency,  
 262 since the model is decomposed into simple time series components, which can be visually inspected.  
 263 Moreover, they do not rely on differencing or moving averages, which make them more transparent than  
 264 other autoregressive moving average models. The third key feature is the ability to incorporate regressors  
 265 (covariates) as explanatory variables in the model. This feature is beneficial to include climate change  
 266 impacts on chlorophyll-a trajectories from solar radiation and air temperature.

In this study an existing Bayesian structural time series modelling framework is customized to our purpose, which is the Prophet forecasting model [33]. This is a decomposable time series model with trend, seasonality and additional regressor component, as well as error term as the main model components:

$$y(t) = g(t) + l(t) + \epsilon(t).$$

267 where, at time  $t$ ,  $y(t)$  is the response variable (chlorophyll-a concentration),  $g(t)$  is a piecewise linear trend  
 268 model,  $l(t)$  is a linear component representing seasonality and additional regressors, and  $\epsilon(t)$  is the error  
 269 term (independent and identically distributed noise). In order to avoid negatively predicted values, the  
 270 natural logarithm of the response variable was taken in the model, and the prediction was then transformed  
 271 back to its original scale by using the exponential function. An advantage of the Prophet model is that it  
 272 can handle irregular intervals, which is important as our fused chlorophyll-a observations are not regularly  
 273 spaced.

274 Here we briefly introduce the model without aiming completeness; for the full model formulation the  
 275 reader is referred to [33]. We use a piecewise linear model with a constant rate of growth and change  
 276 points. Suppose there are  $S$  change points, over a history of  $T$  points, at times  $s_j, j = 1, \dots, S$ . We define

277 a vector of rate adjustments  $\delta \in \mathbb{R}^S$ , where  $\delta_j$  is the change in rate that occurs at time  $s_j$ . The rate at any  
 278 time  $t$  is then the base rate  $k$ , plus all of the adjustments up to that point, which is represented by a vector  
 279  $\mathbf{a}(t) \in \{0, 1\}^S$  such that

$$a_j(t) = \begin{cases} 1, & \text{if } t \geq s_j, \\ 0, & \text{otherwise.} \end{cases}$$

The piecewise linear trend model with change points is then

$$g(t) = (k + \mathbf{a}(t)^T \boldsymbol{\delta}) t + (m + \mathbf{a}(t)^T \boldsymbol{\gamma})$$

280 where  $k$  is the growth rate,  $\mathbf{a}(t)$  is a change point indicator as defined above,  $\boldsymbol{\delta}$  is the vector of rate  
 281 adjustments,  $m$  is the offset parameter, and to make the function continuous,  $\gamma_j$  is set to  $-s_j \delta_j$ . We employ  
 282 the following prior on  $\boldsymbol{\delta} = (\delta_1, \dots, \delta_S)$ .

$$\delta_j \sim \text{Laplace}(0, \tau)$$

283 where  $\tau$  controls the flexibility of the model in alternating its rate. When the model is used for forecasting,  
 284 the trend has constant rate and the uncertainty in the forecast trend is estimated. Future rate changes are  
 285 simulated that emulate those of the past. In a fully Bayesian framework this can be done with a hierarchical  
 286 prior on  $\tau$  to obtain its posterior. In long-term forecasts, which is our purpose, one of the most influential  
 287 factors is the uncertainty in the future trend. In this model, the uncertainty in the forecast trend is estimated  
 288 by assuming that in the future the same average frequency and magnitude of rate changes will occur as  
 289 observed in the past:

$$\text{for all } j > T, \begin{cases} \delta_j = 0 & \text{with probability } \frac{T-S}{T} \\ \delta_j \sim \text{Laplace}(0, \lambda) & \text{with probability } \frac{S}{T}. \end{cases}$$

290 Once  $\lambda$  has been inferred from the data, we use this model to simulate possible future trends and to compute  
 291 uncertainty intervals. In the seasonality model we approximate seasonal effects with a standard Fourier  
 292 series expansion with chosen periodicity  $P$ , and Fourier order  $n$ . The seasonality model is:

$$s(t) = \sum_{n=1}^N \left( a_n \cos \left( \frac{2\pi n t}{P} \right) + b_n \sin \left( \frac{2\pi n t}{P} \right) \right).$$

293 In this model the following periods are used,  $P = 3652.5$  for decadal periodicity,  $P = 365.25$  for yearly  
 294 periodicity,  $P = 182.625$  for half-yearly periodicity, and  $P = 91.3125$  for quarterly periodicity (in days).  
 295 The Fourier order was chosen as  $N = 10$  after tuning such that under-fitting and over-fitting is avoided by  
 296 minimizing the test error. The linear component then becomes

$$l(t) = X(t)\beta$$

297 where  $X(t) = [\cos(\frac{2\pi 1t}{P}), \sin(\frac{2\pi 1t}{P}), \dots, \cos(\frac{2\pi Nt}{P}), \sin(\frac{2\pi Nt}{P}), R_1(t), \dots, R_J(t)]$  is a matrix of  
 298 seasonal components  $s(t)$  and additional vectors of regressors, while  $\beta = [a_1, b_1, \dots, a_N, b_N, r_1, \dots, r_J]^T$   
 299 includes the  $2N$  parameters of the Fourier series expansion and the  $R$  regression coefficients of the  
 300 additional explanatory variables. The following  $\beta \sim N(0, \sigma^2)$  prior is imposed independently on each  
 301 component of  $\beta$ . By default the linear component of the model only contains features for modeling  
 302 seasonality but through specifying covariates ("regressors") we can include additional arbitrary vectors to  
 303  $X(t)$  whose regression coefficients will be inferred. Combining the trend, seasonality and error components  
 304 the final model becomes:

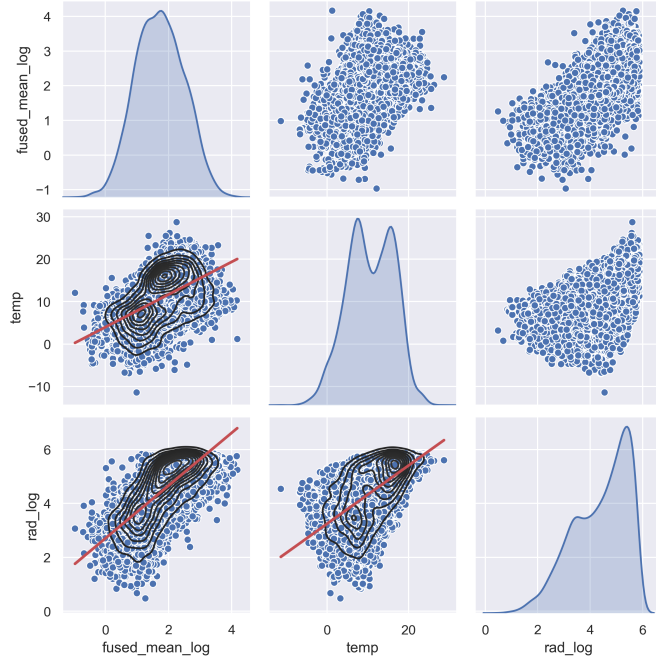


**Figure 5.** Pair plots of the log transformed response variable (fused chlorophyll-a), and the explanatory variables (log transformed radiation and temperature). Scatter plots are shown together with Kernel Density Estimates (black) and linear regression (red).

$$y(t) | m, \delta, \beta, \sigma \sim N(g(t) + l(t), \sigma)$$

305 In order to construct an appropriate structural time series model, the selection of model components was  
 306 facilitated by exploratory analysis steps, such as seasonal shape extraction, investigating the correlation  
 307 of explanatory and response variables (Figure 5), produce periodogram and wavelet analysis to explore  
 308 periodicity, and perform time series decomposition. Apart from chlorophyll-a, the solar radiation regressor  
 309 data is also log transformed, since that produces a correlation structure to log chlorophyll, which is closer  
 310 to linearity (see Figure 5). The temperature data could not be log transformed as it contains negative values.  
 311 The continuous wavelet power spectrum revealed a persistent 12-month periodicity, which explained the  
 312 largest amount of variability over the sampling period, while the rest of the variability is attributed to  
 313 6-month and 3-month periodicity. This is in line with previous research findings of wavelet analysis for the  
 314 same observation station [37].

315 In the current structural time series model implementation the following components are used. Linear  
 316 trend with change points (change point prior scale is defined), multi-period seasonality: decadal, yearly,  
 317 half-yearly, and quarterly (periodicity, Fourier order, and prior scale are defined), as well as four additional  
 318 regressors (air temperature, solar radiation, and their lag1). It should be noted, that adding more than lag1  
 319 of the regressors did not improve the prediction further. The parameter inference can be either done by  
 320 optimization, using Limited-memory Broyden–Fletcher–Goldfarb–Shanno algorithm (L-BFGS) to find a  
 321 maximum a posteriori estimate, or through full posterior inference to include model parameter uncertainty  
 322 in the forecast uncertainty.

## 323 2.4 Tracking phytoplankton spring bloom dynamics

324 Since the methodological framework focuses on phytoplankton phenology as derived quantity, obtained  
 325 from the chlorophyll-a concentration time series, the proposed feature extraction method is presented in  
 326 this section. In order to track the evolution of phytoplankton spring bloom we propose to derive the cardinal  
 327 dates using a non-parametric shape constrained method, namely concave regression [9, 14, 13]. The concave  
 328 or convex regression setup for a data set of size  $\{n : (x_i, y_i) : i = 1, \dots, n\}$  where  $x_1 < x_2 < \dots < x_n$  is  
 329 the following:

$$Y_i = r_0(x_i) + \epsilon_i$$

330 for a concave function  $r_0$  on  $\mathbb{R}$ , where  $\{\epsilon_i : i = 1, \dots, n\}$  are independent and identically distributed  
 331 random variables and  $Y_i$  is the log chlorophyll-a concentration. Then, we apply concave regression on the  
 332 log chlorophyll-a concentration data. We assume that the target of the estimation,  $r_0 : \mathbb{R} \rightarrow \mathbb{R}$ , is concave.  
 333 Writing  $\mathcal{K}$  for the set of concave functions on  $\mathbb{R}$ , the least squares estimate of  $r_0$  is

$$\operatorname{argmin}_{r \in \mathcal{K}} \Phi(r), \quad \text{where } \Phi(r) = \frac{1}{2} \sum_{i=1}^n (y_i - r(x_i))^2$$

334 Utilizing this concave regression setup, the following two methodological steps are taken to identify the  
 335 spring bloom cardinal dates (see Figure 6). The cardinal dates are the spring bloom beginning (B), -peak  
 336 (P), and -end (E) dates expressed as the day of the year.  
 337

#### 2.4.1 Isolating the spring bloom

We take yearly time series of log chlorophyll-a concentrations ( $y_t$ ), and assume that it is bi-modal separated by a boundary point  $t_b$ . In order to reduce computation time we omit the first two months ( $t_1 = 60$ ) and last two months ( $t_2 = 300$ ) of the dataset since we know that the boundary that separates the spring and summer bloom will not be found there. Then we fit  $\Phi(t)$  on the data:

$$\Phi(t) = \begin{cases} \varphi_{t_b}(t) & t \leq t_b \\ \tilde{\varphi}_{t_b}(t) & t > t_b \end{cases}$$

338 where  $\varphi_{t_b}(t)$  is the concave regression of  $(x_i, y_i) : x_i \leq t_b$  on  $[t_1, t_b]$ , the "left side", and  $\tilde{\varphi}_{t_b}(t)$  is the  
 339 concave regression of  $(x_i, y_i) : x_i > t_b$  on  $[t_b + 1, t_2]$ , the "right side". Therefore both  $\varphi_{t_b}(t)$  and  $\tilde{\varphi}_{t_b}(t)$   
 340 are concave. The optimal boundary  $t_b^{opt}$  is found where the mean squared error of  $\Phi(t)$  is minimal:

$$t_b^{opt} \rightarrow \operatorname{argmin}_{t_b} MSE_{t_b} + M\tilde{SE}_{t_b}$$

$$MSE_{t_b} = \frac{1}{t_b} \sum_{j=t_1}^{t_b} (y_j - \varphi_{t_b}(t_j))^2$$

$$M\tilde{SE}_{t_b} = \frac{1}{t_2 - t_b} \sum_{j=t_b+1}^{t_2} (y_j - \tilde{\varphi}_{t_b}(t_j))^2$$

341 This process of determining the boundary of spring and summer bloom is visually depicted in Figure 6A  
 342 and Figure 6B.

#### 2.4.2 Derive cardinal dates of the spring bloom

343 After finding the boundary ( $t_b^{opt}$ ) only the spring bloom ("left side") of the data is considered for further  
 344 analysis where  $t \in [0, t_b^{opt}]$ . Then we take a continuous function  $\Phi^*(t)$  which is defined as follows:  
 345

$$\Phi^*(t) = \begin{cases} c_l = \operatorname{mean}(y_t : t \in [0, t_l]) & t \leq t_l \\ \varphi(t) & t_l < t \leq t_r \\ c_r = \operatorname{mean}(y_t : t > t_r) & t > t_r \end{cases}$$

346 where  $c_l$  and  $c_r$  are constant and  $\varphi(t)$  is the concave regression of  $(x_i, y_i) : t_l < x_i \leq t_r$ . The points where  
 347 the left constant function ends and the right constant function starts ( $t_l$  and  $t_r$ ) will become the beginning

348 and the end of the bloom (cardinal dates B and E). The third cardinal date, the peak of the bloom, is where  
 349  $\varphi(t)$  takes its maximum. The points  $t_l$  and  $t_r$  are found where the mean squared error of  $\Phi^*(t)$  is minimal:

$$(t_l, t_r) \rightarrow \operatorname{argmin}_{t_l, t_r} MSE_{cl} + MSE_{cr} + MSE_\varphi$$

$$MSE_{cl} = \frac{1}{t_l} \sum_{j=0}^{t_l} (y_j - c_l(t_j))^2$$

$$MSE_{cr} = \frac{1}{t_J - t_r} \sum_{j=t_r}^{t_J} (y_j - c_r(t_j))^2$$

$$MSE_\varphi = \frac{1}{t_r - t_l} \sum_{j=t_l}^{t_r} (y_j - \varphi(t_j))^2$$

350 This final methodological step to identify  $t_l$  and  $t_r$  is shown in Figure 6C and Figure 6D. Finally, the  
 351 cardinal dates together with the concave regression and the chlorophyll-a time series (transformed back to  
 352 original values by taking their exponential function) are depicted in Figure 6E.

### 3 RESULTS

#### 353 3.1 Long term chlorophyll-a prediction

354 The Bayesian structural time series forecasting model (introduced in Section 2.3.1) was trained (1976-  
 355 2010) and tested (2010-2018) on the fused chlorophyll-a concentration signal and the historical measured  
 356 solar radiation and air temperature data. Figure 7 visually depicts the validation of the in-sample forecast  
 357 (1976-2010) and the forecast (2010-2018) against the fused data. The figure shows that most measurements  
 358 lie within the predictive uncertainty band, indicating the forecasting model's reliability.

359 After the calibration of hyperparameters and initial validation, the time series forecasting model was  
 360 retrained using the entire historical period (1976-2018), to better capture historical trends, and used for  
 361 long-term chlorophyll-a concentration prediction (2019-2089). Since the model contains log transformed  
 362 solar radiation and air temperature as regressors, they need to be provided for the entire forecast period.  
 363 Consequently, after 2019 the bias corrected climate change projections are applied instead of the field  
 364 observations. Given the numerous generated climate change projections (120 were used), the same number  
 365 of future chlorophyll-a concentration trajectories were simulated, as shown in Figure 8. One can observe  
 366 that the predictive uncertainty increases over time as we get farther from the forecast start date. This  
 367 predictive uncertainty originates from the trend component as explained in Section 2.3.1, and the modelling  
 368 choices (e.g. changepoint prior scale) will influence it. We should emphasize that such long term prediction  
 369 is only a simplified approximation of the future chlorophyll-a signal, which follows a piecewise linear trend  
 370 and continues to repeat its multi-seasonal behaviour, learnt from the past data, moreover includes linear  
 371 effects of the two climate variables. These assumptions guarantee fast computation time, thus allowing  
 372 numerous simulations for uncertainty quantification, which is the objective of this study. Nonetheless, it  
 373 does not replace complex physically-based numerical models that are capable of simulating a wide range  
 374 of ecological processes.

#### 375 3.2 Changes in phytoplankton bloom dynamics

376 The feature extraction step to derive the spring bloom cardinal dates (see Section 2.4) is first applied to the  
 377 mean fused chlorophyll-a data to obtain the historical evolution of spring bloom dynamics. Unfortunately,  
 378 the cardinal dates could only be derived starting from 1998. This is due to the fact that between 1976 and  
 379 1998 only in-situ measurements were available which had a sparse temporal sampling frequency (10-20  
 380 per year). As previously argued, this number of yearly data points is insufficient to extract the cardinal  
 381 dates. The historical phytoplankton bloom dynamics from 1998 to 2018 is depicted in Figure 9. The figure  
 382 displays the three cardinal dates (beginning - green, peak - red, end - blue), the bloom duration (shaded

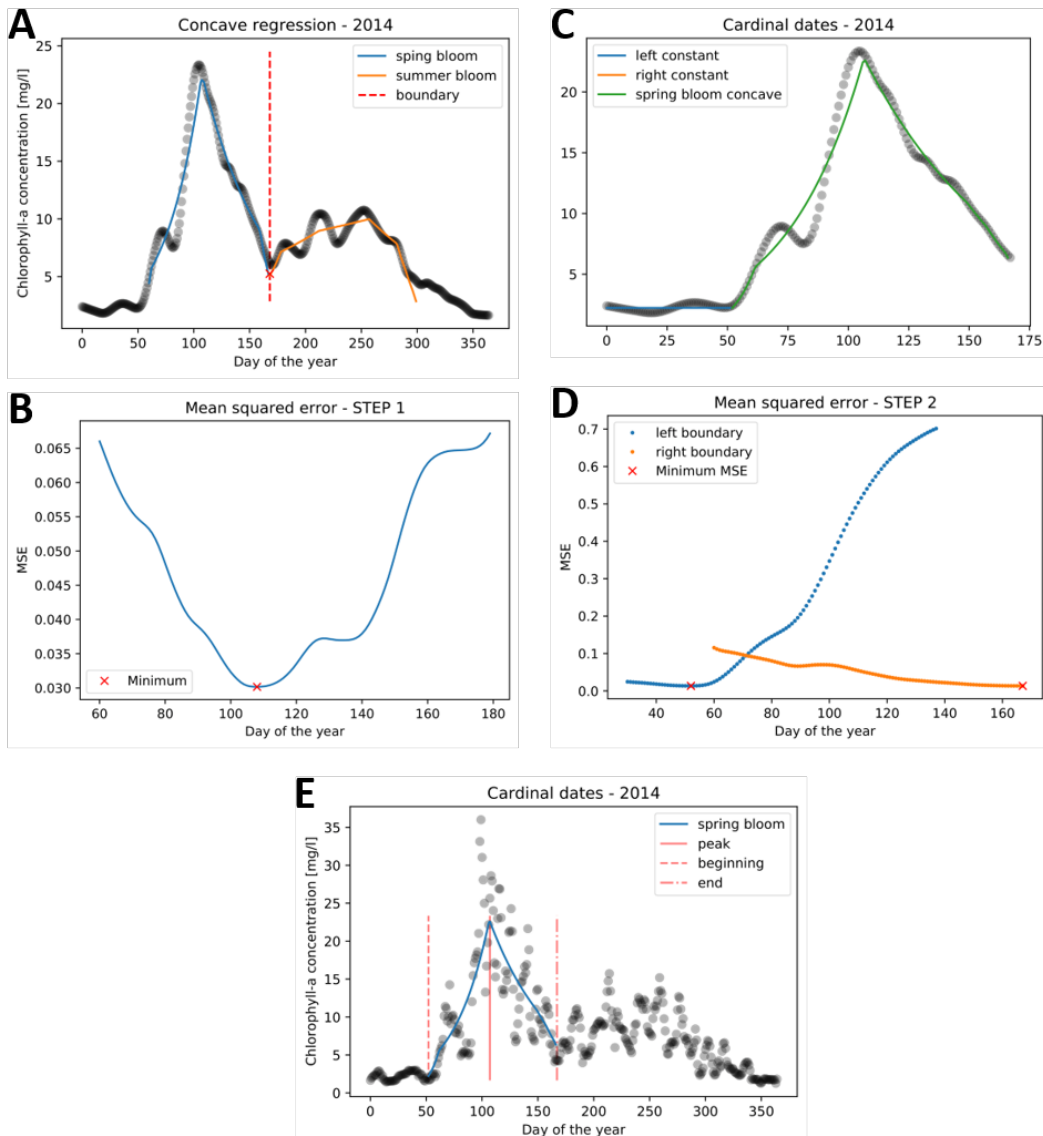


**Figure 6.** Steps to derive the cardinal dates of phytoplankton spring blooms: (1) Determining the boundary ( $t_b$ ) for isolating the spring bloom (A-B), and (2) concave regression to spring bloom (C-D). The cardinal dates of the spring bloom are shown in (E).

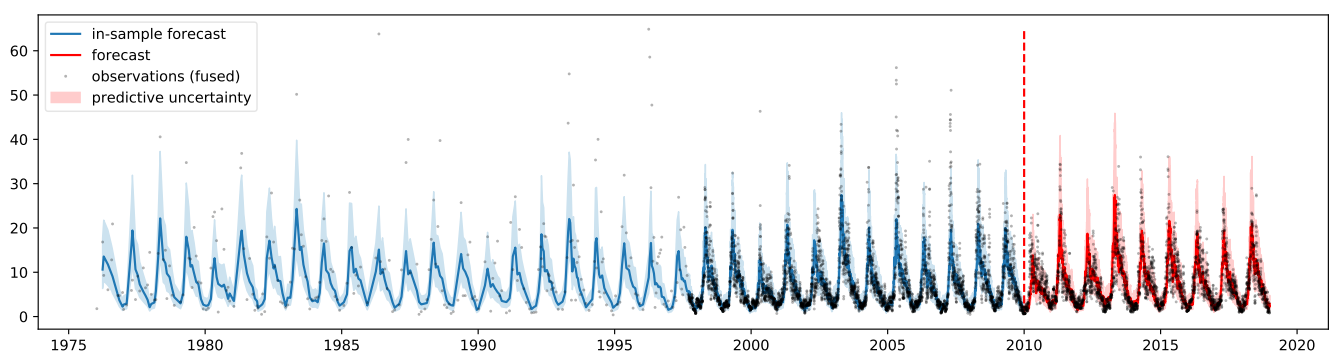


**Figure 7.** Time series forecasting validation against fused observations. Model fit between 1976-2010 (blue) and forecast between 2010-2018 (red). Predictive uncertainties in shaded area.

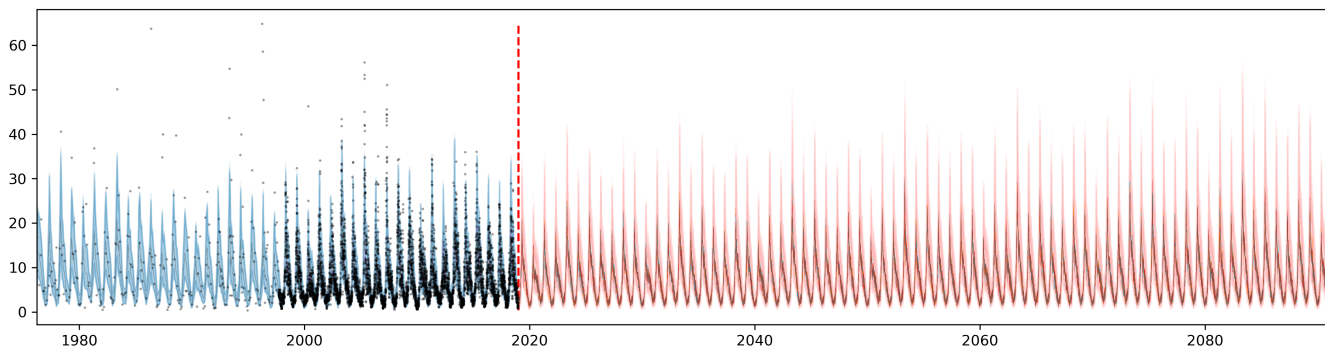


**Figure 8.** Long term chlorophyll-a concentration time series forecasting with radiation and temperature explanatory variables from generated climate projections (based on Euro-CORDEX). 120 solar radiation and air temperature projection scenarios were used to produce the 120 chlorophyll-a trajectories. Model fit between 1976-2018 (blue) and forecast between 2019-2089 (red). Predictive uncertainty in shaded area.

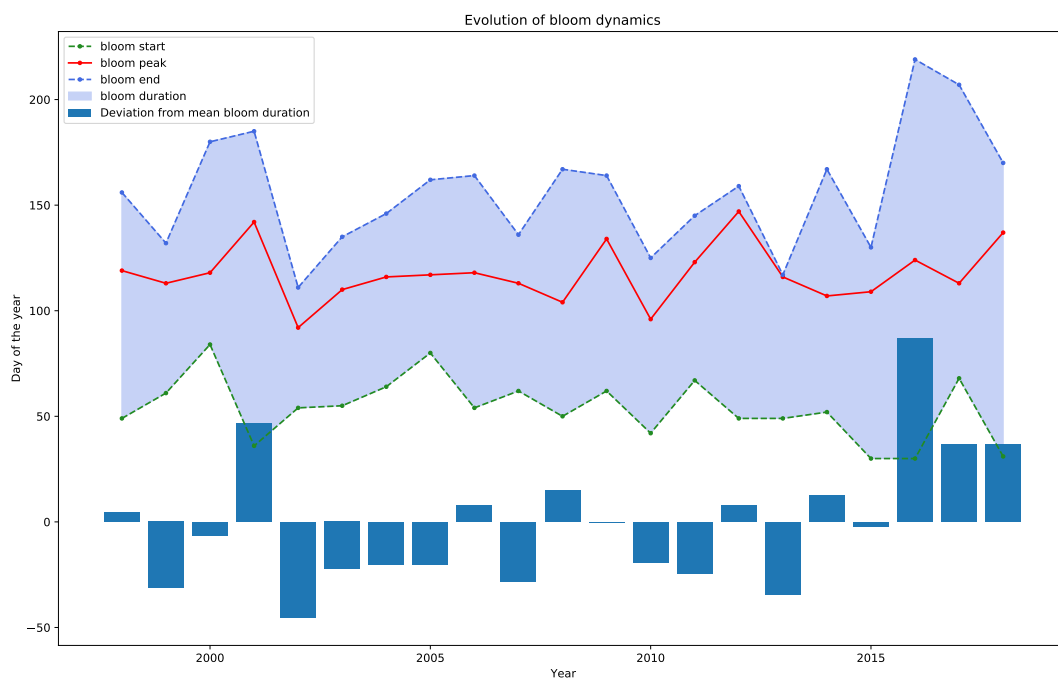


**Figure 9.** Historical spring bloom cardinal dates (beginning - green, peak - red, end - blue) and bloom duration (shaded blue area). The bar chart shows the yearly deviation (anomaly) from the long-term mean bloom duration.

383 blue area), and the bloom duration anomaly from the long-term mean bloom duration (bar chart). It can  
 384 be observed that for certain years (2002, 2012, 2013) the bloom peak and bloom end cardinal dates lie  
 385 very close to each other. These instances were visually confirmed. It was found that for 2002 and 2012 the  
 386 feature extraction algorithm was accurate as a fast decay followed the bloom peak. On the other hand, in  
 387 2013 there was visibly no spring bloom observed, only a dominant summer bloom. This led the algorithm  
 388 to falsely identify the spring bloom peak and end. This finding suggests that years where no spring bloom  
 389 is observed should be removed from the dataset prior to applying the spring bloom cardinal detection  
 390 algorithm.

391 The feature extraction steps are then repeated on the projected future chlorophyll-a concentration between  
 392 2019-2089. The predicted future spring bloom cardinal dates are depicted as boxplots in Figure 10A and  
 393 as histograms in Figure 10B. The results indicate a relatively small variation in the predicted bloom peak  
 394 timing (see Figure 11B), while a much higher level of uncertainty is observed for the bloom beginning

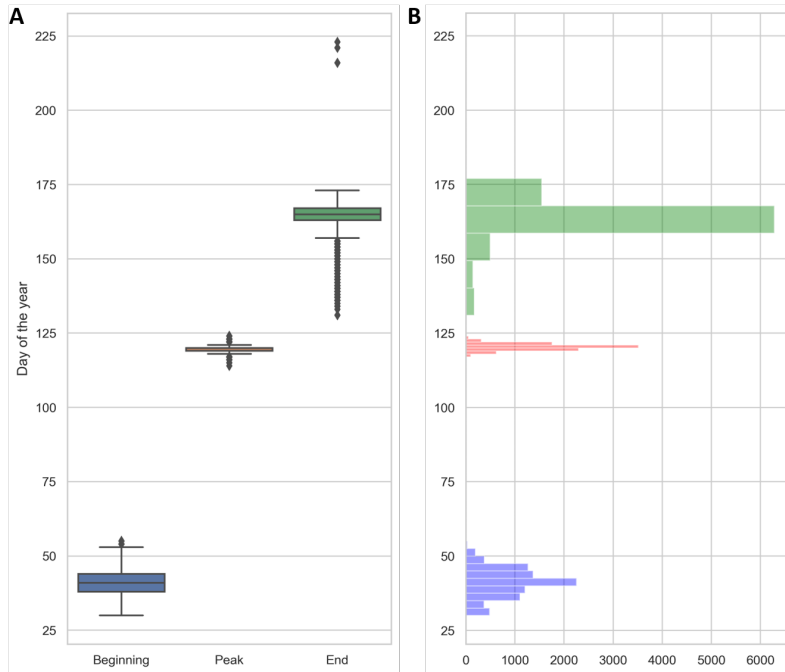


**Figure 10.** Range of predicted future bloom cardinal dates (**A**) and their distributions (**B**) under 120 generated radiation and temperature projections (based Euro-CORDEX) (2019–2089). The cardinal dates are bloom beginning (blue), -peak (red), and -end (green).

395 (see Figure 11A) and end timing (see Figure 11C). The bloom beginning is predicted to slightly but  
 396 consistently shift earlier, resulting in longer bloom duration towards the end of the century (see Figure  
 397 12A). The earlier spring bloom as an effect of climate change is in line with previous findings by [21]  
 398 and [36] in laboratory trials (mesocosm experiments), by [8, 16, 27, 11] using historical data, or by  
 399 [12] using numerical (hydrodynamic and ecological) prediction models forced by future climate change  
 400 scenarios. Many of these studies found an even higher rate of spring bloom forward shift but in our case  
 401 the accelerating effect of temperature rise might be moderated by the decreasing solar radiation trend. We  
 402 emphasize that the actual day of the year of the derived cardinal dates may not be comparable to other  
 403 findings in literature, since we used another method to obtain these cardinal dates. Thus, the observed  
 404 trends and uncertainties carry the most value. We should also point out that the predicted earlier spring  
 405 blooms may not be a simple climatic response but could be the result of complex processes (physical and  
 406 non-physical). Further investigation of these processes is necessary to fully understand the underlying  
 407 mechanisms causing shifts in phytoplankton dynamics [16].

408 Apart from the cardinal dates, the chlorophyll-a concentration magnitude was also investigated. As Figure  
 409 12B shows, at the end of the 21<sup>st</sup> century higher spring bloom peak magnitude can be expected. Considering  
 410 the ensemble mean values, a  $0.4\% \text{year}^{-1}$  trend is projected. This trend magnitude is comparable with the  
 411 latest findings on chlorophyll-a historical trends in the North-West Shelf regions ( $0.4 - 0.96\% \text{year}^{-1}$ ) [15],  
 412 noting that this estimate was considering offshore marine waters, not coastal zones. It is also comparable to  
 413 [39] who found nearly 20-30 % chlorophyll increase in the same study area between 1987-2012. Various  
 414 numerical studies using climate models also project moderate increase in daily mean net primary production  
 415 between 1980–1999 and 2080–2099 in the shallower southern North Sea [17, 18, 28]. We must emphasize  
 416 that increasing chlorophyll concentration due to climate change is highly region specific (only occurring in  
 417 some coastal areas) and very much debated [39]. In fact, some studies only report shift in spring bloom  
 418 timing and species composition, but not in magnitude. In our study the projected positive trend is most  
 419 probably driven by the linear trend component of the time series model and the rising air temperature  
 420 as regressor, which have positive correlation to chlorophyll, based on the historical data. It should be  
 421 noted, that in reality the correlation between air temperature and chlorophyll-a is non-linear and seasonally  
 422 varying, moreover, it is different on a species or aggregate level. As the time series forecasting model

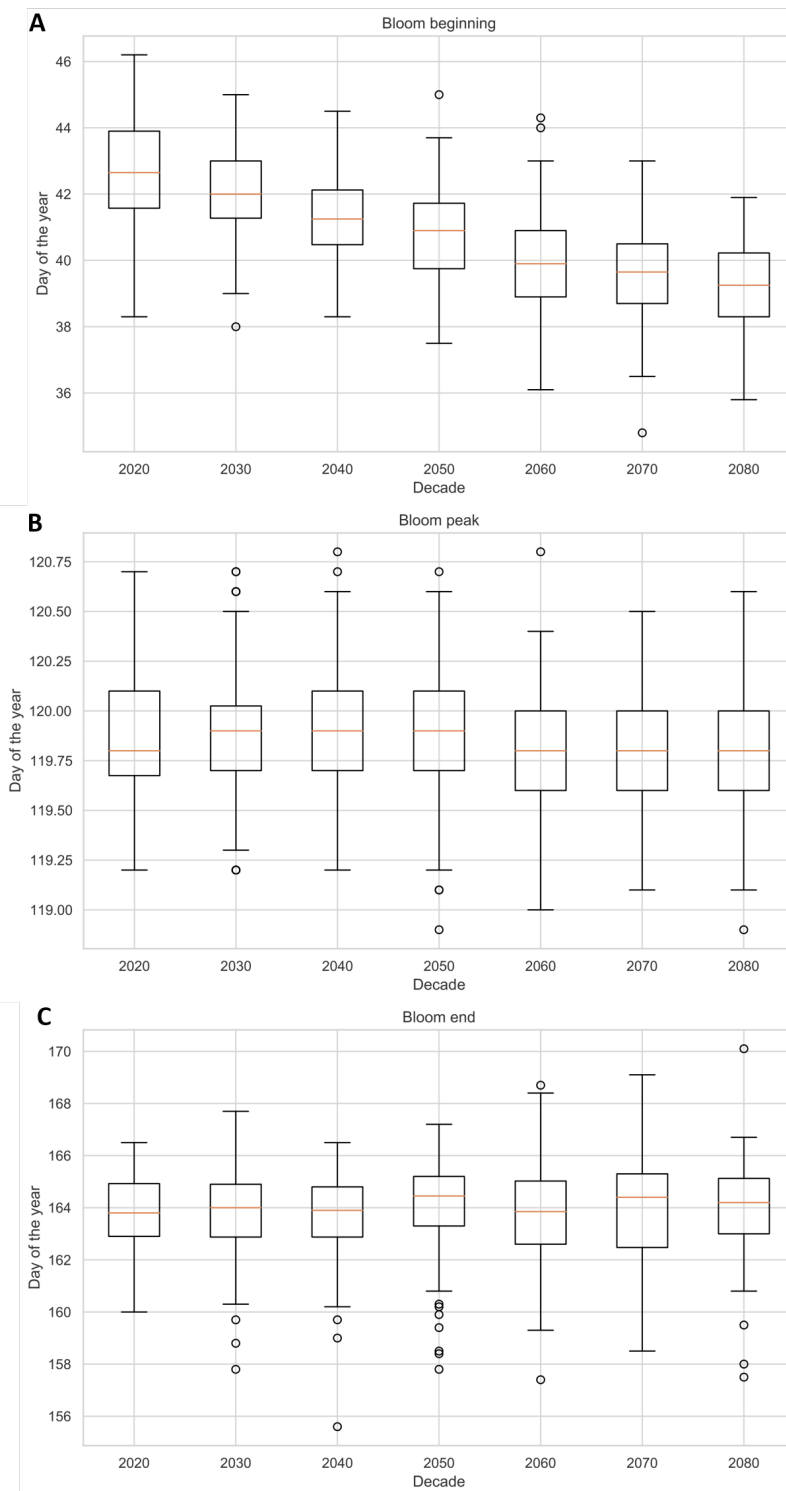


**Figure 11.** Predicted future phytoplankton spring bloom beginning (A), peak timing (B), and end (C) under generated radiation and temperature projections (based Euro-CORDEX) (2019–2089).

423 could not incorporate non-linear correlations, it is assumed linear, hence, simulated interactions are only  
 424 approximations of the real conditions. Nevertheless, in the season of interest (spring), when air temperature  
 425 and solar radiation values did not reach their peak, this correlation is positive and the linearity assumption  
 426 is a good approximation (see Figure 5). Furthermore, with chlorophyll-a concentration as a proxy we aim  
 427 to describe aggregate level response, rather than species level response.

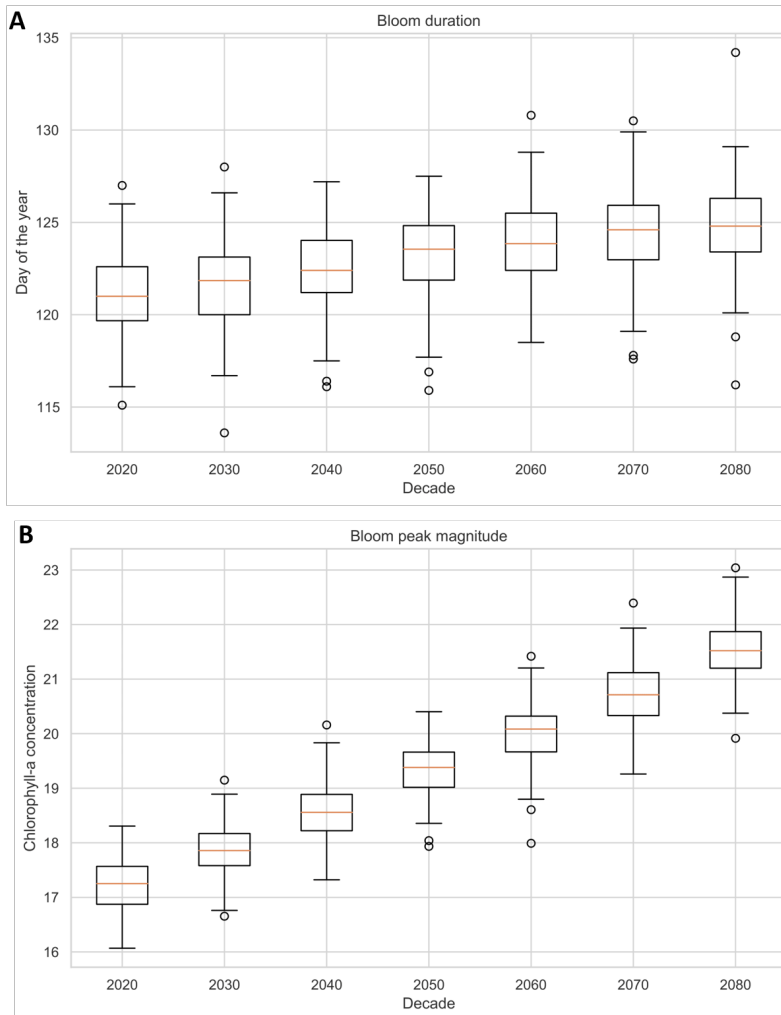


**Figure 12.** Predicted future phytoplankton spring bloom duration (A) and peak magnitude (B) under generated radiation and temperature projections (based Euro-CORDEX) (2019-2089).

## 4 DISCUSSION

428 This paper presents an approach to study observed past and projected future marine phytoplankton  
 429 phenology making use of statistical techniques, rather than physically-based models. The Bayesian setup  
 430 in the data fusion and time series prediction models offer flexibility in model formulation and allow  
 431 characterisation of predictive uncertainties, which is crucial in climate change impact studies. In addition,  
 432 for the extraction of phytoplankton cardinal dates we proposed a non-parametric regression model under  
 433 shape constraints which has not been used before for such purposes, to our knowledge. Regarding the  
 434 applied data, we aimed to make best use of the cross-disciplinary and multi-sourced measurements, covering  
 435 marine biogeochemistry and atmospheric variables from field measurements, satellite imagery, numerical  
 436 models, and synthetic generated scenarios.

437 We acknowledge the various sources of uncertainties in the data and models, which are considered and  
 438 statistically quantified where possible. Firstly, uncertainty in the fusion of chlorophyll-a observations  
 439 is quantified by the posterior distributions obtained through Bayesian parameter inference. Secondly,  
 440 uncertainties in the climate projections are addressed using a large ensemble of generated stochastic  
 441 scenarios, which cover numerous possible trajectories. Thirdly, in the Bayesian time series forecasting  
 442 model we quantify uncertainties in two ways. On the one hand, uncertainty intervals of the future trend are  
 443 computed individually for each projection, and on the other hand, this is repeated for a large number of  
 444 projections, resulting in predictive uncertainty bands for each trajectory and for the entire ensemble. Lastly,  
 445 uncertainty quantification in the feature extraction step is not possible explicitly, nevertheless, thanks to the

446 ensemble approach a range of potential phytoplankton phenologies are simulated over the course of the  
447 21<sup>st</sup> century.

448 The main findings regarding phytoplankton phenology, the projected uncertainties in the beginning  
449 and the end of the spring bloom, as well as the prolonged bloom duration and its forward shift (earlier  
450 bloom), may have repercussions on the marine food web. A consequence could be that energy transfer to  
451 higher trophic levels is disrupted. Such consequences are often described with the trophic match-mismatch  
452 hypothesis of [6]. Based on this hypothesis the reproductive success of higher trophic levels will be best  
453 when the phytoplankton phenology matches their requirements. Phenological shifts may therefore cause  
454 a temporal mismatch between zooplankton consumption and phytoplankton production peak leading to  
455 higher mortality. The severity of these adverse effects in temperate productive systems is, however, debated  
456 [3]. Due to already high natural variability in the timing of predator consumption and its prey in temperate  
457 marine systems, compensating mechanisms may exist that could potentially reduce the impact of the  
458 projected planktonic phenological shift [3].

459 For future research the authors recommend to merge three components of the methodological framework  
460 into a single model. Integrating the Bayesian stochastic climate generator, the Bayesian data fusion model,  
461 and the Bayesian structural time series model would provide a consistent Bayesian hierarchical model that  
462 eliminates redundancies and offers a more elegant solution. It is worth noting that this integrated solution  
463 would be harder to re-use for researchers who are interested to take advantage of only a part of the model  
464 (stochastic generator, data fusion or forecasting) rather than the full chain. A further recommendation  
465 is to extend the approach to include spatial correlations, since currently only one location is considered.  
466 Extending the methodology in this way would allow us to make better use of the multi-dimensional data  
467 structure and include spatial gradients from coast to offshore locations.

468 Finally and most importantly, we recognize that our results related to climate change impacts on spring  
469 bloom dynamics will not resolve the ongoing debate on the complex and often contradictory findings.  
470 Especially, given the fact that the proposed data driven approach neglects the complicated and often  
471 non-linear ecological processes on species level. We reduced the marine biogeochemical response to  
472 climate change into a simple cause-effect relationship between two climate variables (air temperature and  
473 solar radiation) and chlorophyll-a concentration. As a consequence, our results are only an extrapolation  
474 of the observed correlations given projected changes in the climate using statistical models and giving  
475 appropriate attention to uncertainty quantification. Along with these points, we should also mention another  
476 important source of uncertainty in future climate studies focusing on the coastal zone, which is the role  
477 of anthropogenic interventions. Such interventions may include coastal zone management and efforts to  
478 limit eutrophication through reducing nutrient loads in major rivers. In shallow coastal locations these  
479 uncertainties from anthropogenic impacts may outweigh the climate change induced ones, while moving  
480 towards transitional and offshore waters the effects are less prominent. Nonetheless, in this research  
481 human impacts are not addressed, only climatic ones. Despite the limitations, we believe that our proposed  
482 approach contributes to an integrated understanding of ecological responses to variable climate change  
483 through expressing future likelihoods of projected spring bloom dynamics and through the enhanced  
484 characterization of uncertainties associated to data and statistical methods.

## CONFLICT OF INTEREST STATEMENT

485 The authors declare that the research was conducted in the absence of any commercial or financial  
486 relationships that could be construed as a potential conflict of interest.

## AUTHOR CONTRIBUTIONS

487 The study was conducted within the PhD research of LM. LM led the data collection, data and results  
488 analysis, and manuscript preparation. FvdM is the author of Section 2.2 on data fusion, he developed the  
489 data fusion algorithm and executed the computations. GJ provided advice on the use of concave regression  
490 for spring bloom cardinal date extraction and contributed to its mathematical formulation in Section 2.4.  
491 GES advised on the ecological aspects and helped to refine the research objective in order to ensure its  
492 applicability to the journal. All authors contributed to the study conception, design and the discussion of  
493 results and recommendations. All authors read and approved the final manuscript.

## FUNDING

494 This research has received funding from the European Union's Horizon 2020 research and innovation  
495 programme under grant agreement No 727277.

## ACKNOWLEDGMENTS

496 This is a short text to acknowledge the contributions of specific colleagues, institutions, or agencies that  
497 aided the efforts of the authors.

## SUPPLEMENTAL DATA

498 Supplementary Material should be uploaded separately on submission, if there are Supplementary Figures,  
499 please include the caption in the same file as the figure. LaTeX Supplementary Material templates can be  
500 found in the Frontiers LaTeX folder.

## DATA AVAILABILITY STATEMENT

501 The datasets analyzed in this study can be found via the following URLs:  
502 <https://marine.copernicus.eu/>;  
503 <http://projects.knmi.nl/klimatologie/>;  
504 <https://waterinfo.rws.nl>  
505 [http://data.dta.cnr.it/ecopotential/wadden\\_sea/](http://data.dta.cnr.it/ecopotential/wadden_sea/).

506 **Code availability**

507 The Julia and R scripts used for the data fusion can be accessed at:

508 <https://github.com/fmeulen/DataFusion>

509 The Python scripts used for data processing and analysis can be accessed at: <https://github.com/lorincmeszaros/spring-bloom-dynamics>  
510

## 5 APPENDIX

511 The Forward Filtering Backwards Sampling (FFBS)-algorithm steps [5, 31] are defined as follows, where  
 512 the dynamic and measurement models are:

$$\begin{aligned}x_k &= A_{k-1}x_{k-1} + a_{k-1} + N(0, Q_{k-1}) \\y_k &= H_kx_k + N(0, R_k)\end{aligned}$$

513 where  $x_k \in R^n$  is the state,  $y_k \in R^m$  is the measurement,  $N(0, Q_{k-1})$  is the process noise,  $N(0, R_k)$  is  
 514 the measurement noise,  $A_{k-1}$  is the transition matrix of the dynamic model,  $H_k$  is the measurement model  
 515 matrix, and the prior Gaussian  $x_0 \sim N(m_0, P_0)$ . The model can be written in probabilistic terms:

$$\begin{aligned}p(x_k | x_{k-1}) &= N(x_k | A_{k-1}x_{k-1} + a_{k-1}, Q_{k-1}) \\p(y_k | x_k) &= N(y_k | H_kx_k, R_k).\end{aligned}$$

516 This implies that there exist vectors  $m_k^-$  and  $m_k$ , and matrices  $P_k^-, P_k, S_k^-$  such that

$$\begin{aligned}p(x_k | y_{1:k-1}) &= N(x_k | m_k^-, P_k^-) \\p(x_k | y_{1:k}) &= N(x_k | m_k, P_k) \\p(y_k | y_{1:k-1}) &= N(y_k | H_km_k^-, S_k^-)\end{aligned}$$

517 Then the prediction and update steps are the following, where the the recursion is started from the prior  
 518 mean  $m_0$  and covariance  $P_0$ .

519 For  $k \geq 1$

Prediction steps

$$\begin{aligned}m_k^- &= A_{k-1}m_{k-1} + a_{k-1} \\P_k^- &= A_{k-1}P_{k-1}A_{k-1}^T + Q_{k-1}\end{aligned}$$

Update steps

$$\begin{aligned}v_k &= y_k - H_km_k^- \\S_k &= H_kP_k^-H_k^T + R_k \\K_k &= P_k^-H_k^TS_k^{-1} \\m_k &= m_k^- + K_kv_k \\P_k &= P_k^- - K_kS_kK_k^T\end{aligned}$$

Backward sampling:

$$\begin{aligned}G_k &= P_kA_k^T[P_{k+1}^-]^{-1} \\m_k^s &= m_k + G_k[y_{k+1} - m_{k+1}^-] \\P_k^s &= P_k - G_kP_{k+1}^-G_k^T\end{aligned}$$

## REFERENCES

- 520 [1] Alvarez-Fernandez, S. and Riegman, R. (2014). Chlorophyll in North Sea coastal and offshore waters  
521 does not reflect long term trends of phytoplankton biomass. *Journal of Sea Research* 91, 35–44.  
522 doi:10.1016/j.seares.2014.04.005
- 523 [2] Amengual, A., Homar, V., Romero, R., Alonso, S., and Ramis, C. (2012). A statistical adjustment  
524 of regional climate model outputs to local scales: Application to Platja de Palma, Spain. *Journal of  
525 Climate* 25, 939–957. doi:10.1175/JCLI-D-10-05024.1
- 526 [3] Atkinson, A., Harmer, R. A., Widdicombe, C. E., McEvoy, A. J., Smyth, T. J., Cummings, D. G., et al.  
527 (2015). Questioning the role of phenology shifts and trophic mismatching in a planktonic food web.  
528 *Progress in Oceanography* 137, 498–512. doi:10.1016/j.pocean.2015.04.023
- 529 [4] Bartók, B., Wild, M., Folini, D., Lüthi, D., Kotlarski, S., Schär, C., et al. (2017). Projected changes  
530 in surface solar radiation in CMIP5 global climate models and in EURO-CORDEX regional climate  
531 models for Europe. *Climate Dynamics* 49, 2665–2683. doi:10.1007/s00382-016-3471-2
- 532 [5] Carter, C. K. and Kohn, R. (1994). On Gibbs Sampling for State Space Models. *Biometrika* 81, 541.  
533 doi:10.2307/2337125
- 534 [6] Cushing, D. H. (1990). Plankton production and year-class strength in fish populations: An update  
535 of the match/mismatch hypothesis. *Advances in Marine Biology* 26, 249–293. doi:10.1016/  
536 S0065-2881(08)60202-3
- 537 [7] D'Alelio, D., Rampone, S., Cusano, L. M., Morfino, V., Russo, L., Sanseverino, N., et al. (2020).  
538 Machine learning identifies a strong association between warming and reduced primary productivity  
539 in an oligotrophic ocean gyre. *Scientific Reports* 10. doi:10.1038/s41598-020-59989-y
- 540 [8] Desmit, X., Nohe, A., Borges, A. V., Prins, T., De Cauwer, K., Lagring, R., et al. (2020). Changes in  
541 chlorophyll concentration and phenology in the North Sea in relation to de-eutrophication and sea  
542 surface warming. *Limnology and Oceanography* 65, 828–847. doi:10.1002/lno.11351
- 543 [9] Doss, C. R. (2019). Concave regression: value-constrained estimation and likelihood ratio-based  
544 inference. *Mathematical Programming* 174, 5–39. doi:10.1007/s10107-018-1338-5
- 545 [10] Edwards, K. F., Thomas, M. K., Klausmeier, C. A., and Litchman, E. (2016). Phytoplankton growth  
546 and the interaction of light and temperature: A synthesis at the species and community level. *Limnology  
547 and Oceanography* 61, 1232–1244. doi:10.1002/lno.10282
- 548 [11] Edwards, M. and Richardson, A. J. (2004). Impact of climate change on marine pelagic phenology  
549 and trophic mismatch. *Nature* 430. doi:10.1038/nature02808
- 550 [12] Friocourt, Y. F., Skogen, M., Stolte, W., and Albretsen, J. (2012). Marine downscaling of a future  
551 climate scenario in the North Sea and possible effects on dinoflagellate harmful algal blooms. *Food  
552 Additives and Contaminants - Part A Chemistry, Analysis, Control, Exposure and Risk Assessment* 29,  
553 1630–1646. doi:10.1080/19440049.2012.714079
- 554 [13] Groeneboom, P. and Jongbloed, G. (2014). *Nonparametric estimation under shape  
555 constraints: Estimators, algorithms and asymptotics* (Cambridge University Press). doi:10.1017/  
556 CBO9781139020893
- 557 [14] Groeneboom, P., Jongbloed, G., and Wellner, J. A. (2001). Estimation of a convex function:  
558 Characterizations and asymptotic theory. *Annals of Statistics* 29, 1653–1698. doi:10.1214/aos/  
559 1015345958
- 560 [15] Hammond, M. L., Beaulieu, C., Henson, S. A., and Sahu, S. K. (2020). Regional surface chlorophyll  
561 trends and uncertainties in the global ocean. *Scientific Reports* 10. doi:10.1038/s41598-020-72073-9
- 562 [16] Hjerne, O., Hajdu, S., Larsson, U., Downing, A. S., and Winder, M. (2019). Climate Driven Changes  
563 in Timing, Composition and Magnitude of the Baltic Sea Phytoplankton Spring Bloom. *Frontiers in  
564 Marine Science* 6, 482. doi:10.3389/fmars.2019.00482
- 565 [17] Holt, J., Schrum, C., Cannaby, H., Daewel, U., Allen, I., Artioli, Y., et al. (2014). Physical processes  
566 mediating climate change impacts on regional sea ecosystems. *Biogeosciences Discussions* 11,  
567 1909–1975. doi:10.5194/bgd-11-1909-2014
- 568 [18] Holt, J., Schrum, C., Cannaby, H., Daewel, U., Allen, I., Artioli, Y., et al. (2016). Potential impacts of  
569 climate change on the primary production of regional seas: A comparative analysis of five European  
570 seas. *Progress in Oceanography* 140, 91–115. doi:10.1016/j.pocean.2015.11.004
- 571 [19] Jacob, D., Petersen, J., Eggert, B., Alias, A., Christensen, O. B., Bouwer, L. M., et al. (2014).  
572 Euro-cordex: new high-resolution climate change projections for european impact research. *Regional  
573 Environmental Change* 14, 563–578. doi:10.1007/s10113-013-0499-2

- 574 [20] Leutbecher, M. (2019). Ensemble size: How suboptimal is less than infinity? *Quarterly Journal of the*  
575 *Royal Meteorological Society* 145, 107–128. doi:10.1002/qj.3387
- 576 [21] Lewandowska, A. and Sommer, U. (2010). Climate change and the spring bloom: A mesocosm study  
577 on the influence of light and temperature on phytoplankton and mesozooplankton. *Marine Ecology*  
578 *Progress Series* 405, 101–111. doi:10.3354/meps08520
- 579 [22] Llope, M., Chan, K.-S., Ciannelli, L., Reid, P. C., Stige, L. C., and Stenseth, N. C. (2009). Effects  
580 of environmental conditions on the seasonal distribution of phytoplankton biomass in the North Sea.  
581 *Limnology and Oceanography* 54, 512–524. doi:10.4319/lo.2009.54.2.0512
- 582 [23] Luo, Q. (2016). Necessity for post-processing dynamically downscaled climate projections for impact  
583 and adaptation studies. *Stochastic Environmental Research and Risk Assessment* 30, 1835–1850.  
584 doi:10.1007/s00477-016-1233-7
- 585 [24] Mészáros, L., van der Meulen, F., Jongbloed, G., and El Serafy, G. (2020). A Bayesian stochastic  
586 generator to complement existing climate change scenarios: supporting uncertainty quantification in  
587 marine and coastal ecosystems. *Stochastic Environmental Research and Risk Assessment*, 1–18doi:10.  
588 1007/s00477-020-01935-5
- 589 [25] Navarro-Racines, C., Tarapues, J., Thornton, P., Jarvis, A., and Ramirez-Villegas, J. (2020). High-  
590 resolution and bias-corrected CMIP5 projections for climate change impact assessments. *Scientific*  
591 *Data* 7, 1–14. doi:10.1038/s41597-019-0343-8
- 592 [26] Peters, S., Eleveld, M., Pasterkamp, R., van der Woerd, H., DeVolder, M., Jans, S., et al. (2005).  
593 *Atlas of chlorophyll-a concentration for the North Sea (based on MERIS imagery of 2003)*. E-05/01  
594 (Instituut voor Milieuvraagstukken)
- 595 [27] Philippart, C. J. M., van Iperen, J. M., Cadée, G. C., and Zuur, A. F. (2010). Long-term field  
596 observations on seasonality in chlorophyll-a concentrations in a shallow coastal marine ecosystem,  
597 the Wadden Sea. *Estuaries and Coasts* 33, 286–294. doi:10.1007/s12237-009-9236-y
- 598 [28] Pushpadas, D., Schrum, C., and Daewel, U. (2015). Projected climate change impacts on North  
599 Sea and Baltic Sea: CMIP3 and CMIP5 model based scenarios. *Biogeosciences Discussions* 12,  
600 12229–12279. doi:10.5194/bgd-12-12229-2015
- 601 [29] Robert, C. P. and Casella, G. (2004). *Monte Carlo Statistical Methods*. Springer Texts in Statistics  
602 (New York, NY: Springer New York). doi:10.1007/978-1-4757-4145-2
- 603 [30] Rolinski, S., Horn, H., Petzoldt, T., and Paul, L. (2007). Identifying cardinal dates in phytoplankton  
604 time series to enable the analysis of long-term trends. *Oecologia* 153, 997–1008
- 605 [31] Särkkä, S. (2013). *Bayesian Filtering and Smoothing*. Institute of Mathematical Statistics Textbooks  
606 (Cambridge University Press). doi:10.1017/CBO9781139344203
- 607 [32] Schrum, C., Lowe, J., Meier, H. E. M., Grabemann, I., Holt, J., Mathis, M., et al. (2016). *Projected*  
608 *Change—North Sea* (Springer, Cham). doi:10.1007/978-3-319-39745-0\_6
- 609 [33] Taylor, S. J. and Letham, B. (2017). Forecasting at Scale. *PeerJ Inc.* doi:10.7287/peerj.preprints.  
610 3190v2
- 611 [34] van Vuuren, D. P., Edmonds, J., Kainuma, M., Riahi, K., Thomson, A., Hibbard, K., et al. (2011).  
612 The representative concentration pathways: an overview. *Climatic Change* 109, 5. doi:10.1007/  
613 s10584-011-0148-z
- 614 [35] Wiltshire, K. H., Malzahn, A. M., Wirtz, K., Greve, W., Janisch, S., Mangelsdorf, P., et al. (2008).  
615 Resilience of North Sea phytoplankton spring bloom dynamics: An analysis of long-term data at  
616 Helgoland Roads. *Limnology and Oceanography* 53, 1294–1302. doi:10.4319/lo.2008.53.4.1294
- 617 [36] Winder, M., Berger, S. A., Lewandowska, A., Aberle, N., Lengfellner, K., Sommer, U., et al. (2012).  
618 Spring phenological responses of marine and freshwater plankton to changing temperature and light  
619 conditions. *Marine Biology* 159, 2491–2501. doi:10.1007/s00227-012-1964-z
- 620 [37] Winder, M. and Cloern, J. E. (2010). The annual cycles of phytoplankton biomass. *Philosophical*  
621 *Transactions of the Royal Society B: Biological Sciences* 365, 3215–3226. doi:10.1098/rstb.2010.0125
- 622 [38] Winder, M. and Sommer, U. (2012). Phytoplankton response to a changing climate. *Hydrobiologia*  
623 698, 5–16. doi:10.1007/s10750-012-1149-2
- 624 [39] Xu, X., Lemmen, C., and Wirtz, K. W. (2020). Less Nutrients but More Phytoplankton: Long-Term  
625 Ecosystem Dynamics of the Southern North Sea. *Frontiers in Marine Science* 7, 662. doi:10.3389/  
fmars.2020.00662